Accepted manuscript doi:
10.1680/jstbu.22.00219

Accepted manuscript doi:
10.1680/jstbu.22.00219

**Submitted:** 04 November 2022

**Published online in 'accepted manuscript' format:** 16 May 2023

**Manuscript title:** Modelling nonlinear dynamic behaviour of rocking bridge piers with shape memory alloys

**Authors:** Sedef Kocakaplan[1], Ehsan Ahmadi[2] and Mohammad M. Kashani[3]

**Affiliations:** [1]Faculty of Engineering and Natural Sciences, Bursa Technical University, Bursa, Türkiye; [2]Faculty of Engineering and the Built Environment, Birmingham City University, Birmingham, UK and [3]Faculty of Engineering and Physical Sciences, University of Southampton, Southampton, UK

**Corresponding author:** Mohammad M. Kashani, Faculty of Engineering and Physical Sciences, University of Southampton, Southampton, UK.

**E-mail:** mehdi.kashani@soton.ac.uk

Accepted manuscript doi:
10.1680/jstbu.22.00219

## Abstract

In recent years, accelerated bridge construction (ABC) has led to substantial application of precast post-tensioned segmental (PPS) bridge piers. However, PPS piers are not widely used in high-seismicity regions due to their low energy-dissipation capacity. To address this deficiency, this research work examines a series of Shape Memory Alloy (SMA) concrete composite PPS piers. Nonlinear static and dynamic analyses are performed on experimentally validated Finite Element (FE) models of the SMA concrete composite piers, and the results are compared with those without SMA bars. It is found that length, area, and post-tensioning ratio of the SMA bars affect the energy dissipation capacity of the piers, and an optimal design of the bars is required to reach the highest energy dissipation possible. The effects of the SMA bars on the frequency response functions of the piers are investigated for the first time in this study, and it is shown that, unlike the piers without SMA bars, the sub-harmonics and super-harmonics are not seen in the response of the SMA concrete composite piers, mainly for the drift responses. Further, the SMA concrete composite piers experience a significant reduction in the drift responses compared to those without SMA.

**Keywords**: Bridge; composite bridge piers; shape memory alloy; self-centring; post-tensioned; segmental

Accepted manuscript doi:
10.1680/jstbu.22.00219

## 1. Introduction

### *1.1 Background*

In high-seismicity regions, permanent irreversible deformations occur in conventional cast-in-place (CIP) reinforced concrete (RC) piers, and as a result, large residual lateral drift at the bridge deck makes the entire structure non-operational (e.g. non-resilient bridge). Precast post-tensioned segmental (PPS) bridge piers ((Shim et al., 2008), (Dawood et al., 2012)) have been introduced as a suitable substitute to CIP piers in accelerated bridge construction (ABC) ((Mander and Cheng, 1997), (Hewes and Priestley, 2002),(Billington and Yoon, 2004),(Motaref et al., 2014),(Tazarv and Saiid Saiidi, 2016),(Z.B. Haber, 2013)). In addition to the advantages of the offsite manufacturing, which improves concrete casting quality and expedites the construction stages, PPS piers also reduces the residual displacements (Billington et al., 1999) through discrete hinges at the contact surfaces between the segments (i.e., joints) and self-centring mechanism provided by the post-tensioning tendons. The self-centring feature of the piers leads to a more seismically resilient structure, while it should be noted that the segments can still experience local damages at their contact interfaces. Although being a seismically resilient structure, low energy-dissipation capacity of the piers is one of their main deficiencies, and yet remains to be solved for their use in highly seismic zones ((Roh and Reinhorn, 2010), (Ahmadi et al., 2022)).

### *1.2. Energy dissipation improvement*

Recently, to improve energy dissipation capacity of the PPS piers, various strategies have been recommended in the literature (i.e., internal bars and external energy dissipating devices). Ou et al. (Ou et al., 2007) suggested using continuous mild internal steel bars, known as energy-dissipating (ED) bars, across the pier's segments. It was concluded that, if ED bars ratio is below a certain level, the piers exhibit a flag-shape behaviour with reduced residual drifts. Chou and Chen (Chou and Chen, 2006) performed two experimental testing for precast concrete-filled tube segmental bridge columns in which one of the columns included a 5-mm thick A36 Reduced Steel Plate (RSP) at the base as external dissipaters. The researchers showed that equivalent damping ratio of the entire system was highly increased with the use of external dissipaters. Marriott et al. (Marriott et al., 2009) performed experimental studies for an unbonded post-tensioned bridge piers with external, fully replaceable, mild steel hysteretic dissipaters. The authors showed that employed external replaceable dissipaters could improve the energy dissipation capacity of the PPS piers. Other research works also demonstrated high energy dissipation by using external energy dissipating devices (EDD) made of steel angles at the foundation level (ElGawady and Sha'lan, 2011). However, it was observed that adding EDD led to an increase in residual displacement of the piers. Ou et al. (Ou et al., 2010) investigated large-scale precast segmental concrete bridge columns with external conventional ED

Accepted manuscript doi:
10.1680/jstbu.22.00219

bars (as fully bonded and unbonded) and high performance (HP) ED bars (as fully bonded). The authors observed high energy dissipation capacity and reduction in residual drifts of the piers. Additionally, the use of other dissipaters, such as built-in elastomeric pad (Motaref et al., 2010) was also tested. In most of these studies, however, the PPS piers can still experience residual deformations either in the attached energy-dissipating components (can be replaced after a large event), or the structure itself; this means additional maintenance and temporary unserviceability of the structure after severe earthquake events leading to substantial economic losses.

*1.3 Application of SMA*

In recent years, super-elastic Shape Memory Alloy (SMA) bars have been extensively used to improve seismic performance of civil structures (Abdulridha et al., 2013; DesRoches et al., 2004; M Saiid Saiidi; Wang, 2006; N. Mali, 2017; Pereiro-Barceló et al., 2019; Sherif et al., 2018; Song et al., 2006; Speicher et al., 2011). SMA bars dissipate energy of the structure through their nonlinear deformations, and return to their initial state after loading events (i.e. zero residual deformations). Particularly in bridge structures, Valera and Saiidi (S. Varela, 2014) numerically and experimentally studied use of super-elastic Copper-Aluminium-Manganese (CuAlMn) SMA bars in the plastic hinge region of the CIP piers. As a result, limited damage to the plastic hinge region without compromising load-carrying capacity of the pier was found. In another study, Valera and Saiidi (Varela and 'Saiid' Saiidi, 2016) placed unbonded super-elastic Nickel-Titanium (NiTi) SMA bars within a plastic hinge element made of rubber at the base of the CIP piers. A demountable bridge pier, composed of a prefabricated concrete-filled Fibre Reinforced Polymer (FRP) tubes, was also proposed where SMA-equipped cementitious composite plastic hinge was used at the base of the column (Varela and Saiidi, 2017). Roh and Reinhorn (Roh and Reinhorn, 2010) studied the cyclic performance of the PPS piers with SMA bars. In the study, the segments of the PPS piers were connected strongly to each other by using rigid links to prevent the joint openings (leading to a single rocking column), while unbonded SMA bars were provided only at the base segment. The numerical model results showed that piers with SMA bars significantly increased the energy dissipation capacity of the piers and residual drifts were reduced considerably. Moon et al. (Moon et al., 2015), and Roh et al. (H. Roh, 2012) investigated seismic performance of the PPS piers using unbonded martensitic NiTi SMA bars at the bottom segment. Nikbakht et al. (Nikbakht et al., 2015) studied application of SMA bars in PPS piers with steel jacketing tubes at the base segment. Li et al. (Li et al., 2017) also numerically investigated use of SMA bars in the PPS piers equipped with energy-dissipating mild-steel bars. It should be noted that all these studies, which used SMA bars for energy dissipation, were conducted on RC piers regardless of being CIP or PPS.

Accepted manuscript doi:
10.1680/jstbu.22.00219

*1.4 Novelty and contribution*

The preceding literature survey demonstrates that although many experimental and numerical studies have been carried out on energy-dissipation enhancement of PPS piers, there is no detailed parametric study to investigate the nonlinearity of the PPS piers with SMA bars under static and dynamic loadings. Towards achieving a damage-free resilient bridge pier with high energy dissipation capacity, this work numerically investigates the feasibility of an SMA concrete composite PPS pier using a Finite Element (FE) approach through a rigorous parametric study. The concrete segments of the pier are tightened together using post-tensioned stainless-steel tendons. Unbonded post-tensioned super-elastic NiTi SMA bars are used at the edge of the segments to increase energy dissipation and self-centring capacity of the entire pier. Stainless-steel tendons and NiTi SMA bars are highly corrosion resistant. Since there is no carbon steel in the proposed pier, the risk of corrosion is substantially reduced compared to other bridge piers with reinforced carbon steel. These features make the proposed pier to be resilient, durable, and comparatively more environmentally sustainable over its lifetime.

To investigate the effect of SMA bars on the performance of PPS piers, an experimentally validated FE model is developed in OpenSees code (McKenna, 2011). A comprehensive parametric study is performed to understand how post-tensioning tendon and SMA bars affect the energy dissipation capacity of the pier through a series of nonlinear static analyses. From this parametric study, the piers with the highest energy dissipation capacity are selected to be used in nonlinear dynamic analyses. Finally, frequency response functions (FRFs) of the SMA-equipped piers are compared with those without SMA bars for the first time. Frequency response functions could successfully capture the nonlinearity in dynamics of a structural system (e.g., rocking response) ((Kibriya et al., 2018)).

## 2. Finite Element Modelling of the SMA Concrete Composite Piers

*2.1 Segments and tendon*

Different number of segments are considered in this study to represent piers with different aspect ratios. Fig. 1 illustrates an exemplary bridge pier with four segments, and total height of $H$ = 2000 mm. The precast concrete segments have width, $B$ = 500 mm and height, $h$ = 500 mm for all the piers. The pier supports a bridge deck located on top of the segments, modelled as a lumped mass (see Fig. 1a). The other PPS piers studied in this study are composed of two, six, and ten segments.

The individual segments of the pier are tightened together using an unbonded post-tensioning stainless steel tendon (see Fig. 1a and Fig. 1b). The tendon provides a self-centring mechanism in the pier when subjected to lateral loading or any unbalance moment. Unbonded post-tensioned super-elastic NiTi SMA bars are used at the bottom segments to increase energy dissipation capacity of the pier (see Fig. 1a and Fig. 1b). Fig.1b illustrates the arrangement of the SMA bars.

Accepted manuscript doi:
10.1680/jstbu.22.00219

The FE modelling of the pier is shown in Fig. 1d. The two-dimensional (2D) FE model of the pier is developed in the programme OpenSees [22], and its details can be found in Ahmadi et al. (Ahmadi and Kashani, 2020). Elastic Beam-Column elements are used for the modelling of the segments (see Fig. 1d). The segments are connected through nodes with three degrees-of-freedoms: one horizontal translations, one vertical translation, and one rotation. The sliding between segments and accordingly frictional damping is discarded in the modelling. This is because the diameter of the hole within the segment is slightly larger than the tendon diameter, and hence, the segments are not allowed to slide on top of each other. The post-tensioned tendon is modelled with a Truss Element and an Elastic Perfectly Plastic material. An initial strain was implemented into the material model to account for post-tensioning force of the tendon. Yield stress, $\sigma_y$, and elastic modulus of the tendon are 1860 MPa and 200 GPa respectively. For the tendon, post-tensioning is defined as post-tensioning-to-yield stress, $\sigma_t/\sigma_y$. Corotational geometric transformation is used for Beam-Column and Truss elements to account for their geometric nonlinearities. The axial load from the top deck is defined as a ratio of the axial load to the axial capacity of the concrete section, $N/(f_cA_g)$, where $N$ is the axial load, $f_c$ and $A_g$ are the concrete compressive strength and the total cross section area of the segment, respectively. The concrete strength, $f_c$, is taken 35 MPa in this study. Inertial effects of the bridge deck are considered by applying lumped horizontal and vertical masses to the top node of the pier. These masses are equivalent to the axial force acting on the pier.

*2.2 Rocking joints*

Fig. 2 shows detailed modelling of rocking joints for the piers. Fig. 2a and Fig. 2b are for the base and intermediate joints, respectively. The Lobatto Quadrature method (Spieth HA et al., 2004)was adopted to distribute the vertical stiffness of the segments over the compression zones at the contact surfaces between the segments. As shown in Fig. 2c, each compression zone is modelled as a set of axial zero-length spring elements. To simulate the joint openings and compression forces at the contact surfaces, an elastic zero-tension uniaxial material model is assigned to the joints. Further details on the modelling joints in OpenSees can be found in (Ahmadi and Kashani, 2020).

*2.3 SMA bars*

SMA bars can experience large strain and recover to its original shape through stress removal (super-elastic effect) or heating (shape memory effect) ((Li et al., 2017), (Wilson and Wesolowsky, 2005), (DesRoches and Delemont, 2002),(Gholampour and Ozbakkaloglu, 2018)) and provide large energy dissipation through the hysteretic behaviour (Wilson and Wesolowsky, 2005). The self-centring capability of the SMA can cause structures to recover their original position after an earthquake, and thus, can reduce the residual deformation of the structures. The SMA bars have been used in both numerical studies ((Leitner and Hao, 2016), (Shrestha and Hao, 2016)) and experimental works ((S. Saiidi, 2009), (Nan Gao, 2016),(Suhail et al., 2020)) to reduce the residual displacement of structures.

Accepted manuscript doi:
10.1680/jstbu.22.00219

In this research, unbounded post-tensioned super-elastic SMA bars are used at the edge of the segments to increase energy dissipation and self-centring capacities of the entire pier (see Fig. 1d, Fig. 2).

The post-tensioned SMA bars are modelled using Truss Elements. Fig. 3 shows the idealized flag-shape constitutive model used for the SMA (Tazarv and Saiid Saiidi, 2015). As seen in Fig. 3, SMA is a self-centred material, and recovers its original shape after unloading. The tension and compression behaviours are identical. Table 1 summarizes the parameters used for the SMA material model in this work (Li et al., 2017). Post-tensioning ratio of the SMA bars, $\alpha_{SMA}$, is defined as $\sigma_{SMA}^{0}/\sigma_{sAM}$ , where $\sigma_{SMA}^{0}$ is the initial post-tensioning stress in SMA bars, and $\sigma_{sAM}$ is the start stress at austenite-to-martensite transformation phase, $\sigma_{sAM}$ (see Table 1 and Fig. 3). The SMA material model with initial post-tensioning stress was coded and implemented in OpenSees by the authors.

## 3. Numerical Analyses and Discussion

In this section, a parametric study is performed to investigate nonlinear static and dynamic behaviour of the SMA-equipped PPS piers. Nonlinear static analyses are used to investigate the key design parameters: (*i*) number of segments or aspect ratio, (*ii*) length, area, and post-tensioning ratio of the SMA bars, and (*iii*) area and post-tensioning ratio of the tendon, which may affect energy dissipation capacity of the piers.

### *3.1 Nonlinear static analyses*

To explore nonlinear static behaviour of the piers, capacity curves (i.e. base shear verses drift), are obtained for a full cyclic loop (± 6 % drift) and a range of design parameters, as shown in Table 2, and parametric studies are performed as a combination of each design parameter given in the table. As previously defined in section 2, $\alpha_t$ and $\alpha_{sma}$ are post-tensioning ratios of the tendon and SMA bars respectively; $\rho_t$ is the tendon-to-segment area ratio ($A_t/A_c$), and $\rho_{sma}$ is the SMA bars-to-segment area ratio ($A_{sma}/A_c$); $n$ is the number of segments; and $J_{sma}$ is the joint number at which the top node of the SMA bars is located. As shown in Fig. 1a, the bottom end of all SMA bars is connected to the fixed base, and the top end location of the SMA bars varies and is shown by $J_{sma}$. So, $J_{sma}$ represents different length of the SMA bars. The top node of the top segment is taken as the controlling node, and a displacement-control analysis is used to monitor the top displacement, $\Delta$, versus base shear, $V$. The pier's drift is defined as the lateral tip displacement normalised by the total height of the pier, $\Delta/H$. The base shear coefficient is expressed as the base shear normalised by the total weight of the pier, $V/W$. The axial load ratio, $N/(f_cA_c)$, is taken 0.2 for all the analyses.

Fig. 4 shows effects of SMA bars' length, $J_{sma}$, for the piers with different number of segments, $n$, and $\alpha_t$ = 0.4, $\rho_t$ = 0.01, $\alpha_{sma}$ = 0.3, $\rho_{sma}$ = 0.01. Fig. 4a shows the cyclic behaviour of the pier with $n$ = 2 (representing a squat pier) and $J_{sma}$ = 2. $J_{sma}$ = 2 means the length of SMA is half the pier's height. According to the figure, pushover analysis is only performed up to 3.5% drifts as the yielding of the

Accepted manuscript doi:
10.1680/jstbu.22.00219

post-tensioning tendon governs the failure of the pier (Ahmadi and Kashani, 2021). It is seen that the pier exhibits a clear flag-shape behaviour, the enclosed area highlights the energy dissipation capacity of the SMA bars due to their nonlinear deformation. The larger the enclosed area is, the higher the energy dissipation capacity of the pier will be. Further, the zero-residual deformation shows the self-centring capacity of the SMA bars while increasing energy dissipation of the pier. As seen in Fig. 4b, energy dissipation capacity increases when the SMA bars elongate, i.e., $J_{sma}$ increases. Like the piers with no SMA bars, the SMA-equipped piers with $n$ = 3 and $n$ = 4 give no energy dissipation for $J_{sma}$ = 2 (see Fig. 4c and Fig. 4d). As the pier becomes more slender (higher $n$ values here or higher aspect ratio, $H/B$), its initial stiffness and strength drop (Ahmadi and Kashani, 2020). When the SMA bars are very stiff due to their short length, $J_{sma}$ = 2, they do not allow the base segment (the bottom most segment) to rock. Hence, no energy dissipation is seen, and the pier behaves like a pier with one less segment and no SMA bars. For $J_{sma}$ = 3, the SMA bars experience nonlinear deformations, and accordingly enable the pier to dissipate energy (see Fig. 4c and Fig. 4d). For higher $J_{sma}$ values, the energy dissipation capacity of the pier slightly changes (see $J_{sma}$ = 3 in Fig. 4b, $J_{sma}$ = 4, 5 in Fig. 4c and $J_{sma}$ = 5 in Fig. 4d). The reason lies in the fact that the rocking motion of the pier mostly comes from the bottom segments (Ahmadi and Kashani, 2020), and thus, using SMA bars across top segments do not significantly add to the energy dissipation capacity of the pier. So, there is an optimal location or length for the SMA bars, and this optimal location or length increases as the number of segments or aspect ratio of the pier increases. Further, the length of the SMA bars does not change the initial stiffness of the pier.

Hereafter, the pier with four segments is used as an exemplary pier to demonstrate the results throughout this study. However, other piers exhibit similar behaviour. Fig. 5 shows the effect of the SMA bar's area, $\rho_{sma}$, on static behaviour of the exemplary pier with $n$ = 4 for different length of SMA bars, $J_{sma}$. For small area of the SMA bars, $\rho_{sma}$ = 0.005, the pier exhibits a slight energy dissipation. However, energy dissipation of the pier becomes the highest for $\rho_{sma}$ = 0.025 (see Fig. 5b and Fig. 5c). For larger areas of SMA bars, $\rho_{sma}$ = 0.025 and $J_{sma}$ = 2, the pier shows no energy dissipation (see Fig. 5a). This is because the SMA bars become very stiff for large $\rho_{sma}$ and small $J_{sma}$. Thus, like the length of the SMA bars, there is an optimal area of the SMA bars at which the maximum energy dissipation of the pier is reached. Also, the SMA bars' area does not affect the initial stiffness of the pier.

Fig. 6a shows the post-tensioning effect of the SMA bars on the energy dissipation capacity of the exemplary pier. As seen in Fig. 6a, increasing post-tensioning ratio of the SMA bars increases the energy dissipation capacity of the pier. Interestingly, the post-tensioning changes the loading path of the pier. Fig. 6b to Fig. 6d show the stress-strain behaviour of the right-edge SMA bars for different post-tensioning ratios. For the displacement of the pier, the SMA bars exhibit both linear and nonlinear behaviours. However, increasing the post-tensioning ratio reduces the linear behaviour and

increases the nonlinear behaviour, where a higher energy dissipation capacity is reached (see Fig. 6b to Fig. 6d). Particularly at $\alpha_{sma}$ = 0.6, the linear behaviour vanishes, and only nonlinear component contributes to the behaviour of the entire pier (Fig. 5d). Additionally, like the tendon (Ahmadi and Kashani, 2020), the post-tensioning ratio of the SMA bars have no effects on the initial stiffness of the pier.

Fig. 7 shows the effects of the tendon on the energy dissipation capacity of the exemplary pier. Although higher post-tensioning ratio increases the lateral strength of the pier, the energy dissipation capacity of the pier remains almost unchanged (Fig. 7a). Like the post-tensioning effect, increasing tendon's area increases the lateral strength of the pier; however, no change in the energy dissipation of the pier is seen. Thus, generally, the tendon does not affect the energy dissipation capacity of the piers.

To have a better insight into effects of the design parameters on the energy dissipation of the piers, the area enclosed by their cyclic behavior is determined, and taken as an indicator for the dissipated energy of the pier. Fig. 8 shows the contour plots of the dissipated energy for the exemplary pier with $\alpha_{sma}$ = 0.3 and $J_{sma}$ = 3. The amount of the dissipated energy is determined for a range of tendon's post-tensioning ratios, $\alpha_t$, and SMA bar's area ratios, $\rho_{sma}$. Using the results of the contour plots, six piers with high energy dissipation are selected to be used in the dynamic analyses in the next section (section 3.2). The selection of these piers was based on the observed energy dissipation, SMA ratio and post-tensioning ratio of the SMA bars. These six piers along with their non-SMA counterparts are given in Table 3. Table 3 also gives the first natural frequency of the piers, $f_n$, which will be used in section 3.2. As seen, all the frequency values are very close which emphasizes insignificant effects of the tendon and the SMA bars on the initial stiffness of the piers meaning that the SMA bars do not have any significant influence on the initial stiffness (linear range) prior to the joint opening. However, SMA has an impact on the post-joint opening stiffness (nonlinear range).

*3.2 Nonlinear dynamic analyses*

In this section, to examine nonlinear dynamic behaviour of the SMA-equipped piers, frequency response functions (FRFs) of the piers are determined and compared with those without SMA bars (see Table 3 for the piers considered in this section). Frequency response functions (FRFs) for structural engineering applications are usually generated using a sine-sweep or a sine-dwell (discrete form) input ground motion. In sine-dwell analysis, the frequency is increased by discrete values, giving time to the structure to reach a steady-state response. A numerical algorithm is developed in MATLAB to produce the sine-dwell input excitation and convert time history response of the piers to FRFs in frequency domain. A constant-stiffness Rayleigh damping is used for the piers with damping ratio of 5% for all elements in the models (Ahmadi and Kashani, 2020)

Accepted manuscript doi:
10.1680/jstbu.22.00219

Fig. 9 compares normalised base shear-drift curves for a sinusoidal excitation at the frequency of 2.1 Hz for the pier B0 (no SMA bars) and B1 (SMA bars equipped) with varying amplitudes. As stated in section 3.1, SMA bars add to the stiffness of the pier, and thus, the hysteresis loop for the pier B1 is more stretched across the normalised base shear axis. As the pier B1 initiates rocking at very small drift ratios, it dissipates energy through nonlinear deformations of the SMA bars (e.g., 0.6 %, see Fig. 9a). In contrast, at very small drift ratios, the pier B0 does not exhibit significant energy dissipation (e.g., 0.05 %, see Fig. 9a). However, after drift ratio of around 3%, the B0 pier shows energy dissipation arising from Rayleigh damping of the pier at large drift ratios (dissipated energy is 0.9 %, see Figure 9b). Further, as the loading amplitude increases, the energy dissipation of the pier B1 increases (dissipated energy is 1.0 %, see Figure 9b). This is because the SMA bars experience larger nonlinear deformation, and consequently, adds more to the energy dissipation of the pier. This continues until at loading amplitude of 0.3g (see Fig. 9c), the pier B1 reaches a higher strength, smaller drift, and higher energy dissipation increases (dissipated energy is 1.5 %, see Figure 9c) compared to the pier B0 increases (dissipated energy is 0.8 %, see Figure 9c).

The PPS piers are geometrically nonlinear. So, their response around resonant frequency is unstable. This unstable behaviour requires capturing upper and lower branches of the FRFs of the piers. The upper and lower branches are obtained by performing an increasing and decreasing frequency sine-sweep analyses (Kibriya et al., 2018). Further, in order to capture the upper branch response and system's change, a high-amplitude impulse is applied before using the sine-sweep analysis with decreasing frequency. Fig. 10 shows the process of extracting FRFs of an exemplary SMA-equipped pier (Pier B2) for an excitation amplitude of 0.005g. The response history obtained from the sine-sweep analysis includes a transient response and a steady-state response (see Fig. 10a). Thus, to ensure reaching a steady-state response, the dynamic analysis for each pair of loading frequency and amplitude is performed over a period of 30 sec. The steady-state response is isolated in time domain (Fig. 10b). Finally, the steady-state response is plotted versus the loading frequencies for the lower and upper branches of the response, i.e. FRF (Fig. 10c).

The first natural frequencies, $f_n$, determined from the eigenvalue analysis of the piers are given in Table 3. The FRFs are obtained around the first natural frequency of the piers. So, the loading-to-pier frequency ratio, $f/f_n$, changes between 0.02 to 1.4. To achieve this, a series of dynamic analyses are performed for different loading amplitudes varying from 0.005g to 0.3g.

Accepted manuscript doi:
10.1680/jstbu.22.00219

Acceleration and drift responses could potentially allow to investigate dynamic response of a system such as stiffness, damping and natural frequency. These graphs are known as frequency response function that characterise the nonlinearity in a nonlinear dynamic system. Fig. 11 and Fig. 12 show the FRFs of each pier for acceleration and drift responses, respectively along with their corresponding backbone curves. It is seen that the SMA bar-equipped piers give a higher acceleration response (see Fig. 11) and a lower drift response (see Fig. 12) compared to the piers with no SMA bars. Furthermore, almost all the piers exhibit sub-harmonic responses before their resonant frequency. The pier C0 displays super-harmonics at frequencies higher than the resonant frequency (see Fig. 11g and Fig. 12g). This phenomenon is not seen for the piers with higher stiffness i.e., piers A0 and B0; the pier C0 has the lowest initial post-tensioning ratio for the post-tensioning tendon. For the SMA-equipped piers, the SMA bars introduce additional stiffness to the systems, which might cause the super-harmonics to disappear. Fig. 13 shows the backbone curves of all the piers given in Table 3. The figures highlight the lower drift response of the SMA-equipped piers, which is a great advantage in dynamic performance enhancement of PPS piers using SMA bars.

**4. Conclusions**

The purpose of this study is to model and investigate nonlinear static and dynamic behaviours of SMA concrete composite PPS piers. To achieve this aim, an experimentally validated FE model is used. A parametric study is first conducted on the key design parameters through a series of nonlinear static analyses to investigate energy dissipation capacity of the SMA concrete composite piers. Then, a series of nonlinear dynamic analyses are performed on carefully selected piers from the results of the nonlinear static analyses. The piers without SMA bars are also analysed for comparison.

It was found from the results of nonlinear static analyses that there exists an optimal size and length of the SMA bars, which leads to the highest energy dissipation possible. Furthermore, energy dissipation of the pier increases with increasing post-tensioning ratio of the SMA bars until the pier becomes very stiff. The post-tensioning and the area of the tendon do not affect energy dissipation capacity of the pier. However, as expected, higher post-tensioning and area of the tendon increases lateral strength of the pier.

It was also found from the FRFs that the SMA bars reduce the drift responses of the system. In addition to providing energy dissipation in high-amplitude excitation, the SMA bars increase the stiffness of the system. Both piers with and without SMA bars exhibited subharmonics while super-harmonics were observed only for the piers with the lowest initial post-tensioning ratio. Overall, this study shows promising application of posttensioned-SMA bars in PPS piers for enhancing their nonlinear static and dynamic performance.

**Acknowledgement**

The authors acknowledge the support received by the UK Engineering and Physical Sciences Research Council (EPSRC) for a Prosperous Nation [grant number EP/R039178/1]: *SPINE: Resilience-Based Design of Biologically Inspired Columns for Next-Generation Accelerated Bridge Construction*].

**References**

Abdulridha A, Palermo D, Foo S, et al. (2013) Behavior and modeling of superelastic shape memory alloy reinforced concrete beams. *Engineering Structures* 49: 893–904. DOI: 10.1016/j.engstruct.2012.12.041.

Ahmadi E and Kashani MM (2020) Numerical investigation of nonlinear static and dynamic behaviour of self-centring rocking segmental bridge piers. *Soil Dynamics and Earthquake Engineering* 128(September 2019). Elsevier Ltd: 105876. DOI: 10.1016/j.soildyn.2019.105876.

Ahmadi E and Kashani MM (2021) Seismic vulnerability assessment of precast post-tensioned segmental bridge piers subject to far-fault ground motions. *Structures* 34: 2566–2579. DOI: 10.1016/j.istruc.2021.09.041.

Ahmadi E, Kocakaplan S and Kashani MM (2022) Nonlinear seismic fragility analysis of a resilient precast post-tensioned segmental bridge pier. *Sustainable and Resilient Infrastructure* 7(6). Taylor & Francis: 823–841. DOI: 10.1080/23789689.2022.2082644.

Billington SL and Yoon JK (2004) Cyclic Response of Unbonded Posttensioned Precast Columns with Ductile Fiber-Reinforced Concrete. *Journal of Bridge Engineering* 9(4): 353–363. DOI: 10.1061/(asce)1084-0702(2004)9:4(353).

Billington SL, Barnes RW and Breen JE (1999) A Precast Segmental Substructure System for Standard Bridges. *PCI Journal* 44(4). DOI: 10.15554/pcij.07011999.56.73.

Chou CC and Chen YC (2006) Cyclic tests of post-tensioned precast CFT segmental bridge columns with unbonded strands. *Earthquake Engineering and Structural Dynamics*. DOI: 10.1002/eqe.512.

Dawood H, Elgawady M and Hewes J (2012) Behavior of segmental precast posttensioned bridge piers under lateral loads. *Journal of Bridge Engineering*. DOI: 10.1061/(ASCE)BE.1943-5592.0000252.

DesRoches R and Delemont M (2002) Seismic retrofit of simply supported bridges using shape memory alloys. *Engineering Structures* 24(3): 325–332. DOI: 10.1016/S0141-0296(01)00098-0.

DesRoches R, McCormick J and Delemont M (2004) Cyclic Properties of Superelastic Shape Memory Alloy Wires and Bars. *Journal of Structural Engineering* 130(1): 38–46. DOI: 10.1061/(ASCE)0733-9445(2004)130:1(38).

ElGawady MA and Sha'lan A (2011) Seismic Behavior of Self-Centering Precast Segmental Bridge Bents. *Journal of Bridge Engineering* 16(3). DOI: 10.1061/(ASCE)BE.1943-5592.0000174.

Gholampour A and Ozbakkaloglu T (2018) Understanding the compressive behavior of shape memory alloy (SMA)-confined normal- and high-strength concrete. *Composite Structures* 202: 943–953. DOI: 10.1016/j.compstruct.2018.05.008.

H. Roh AMRJSL (2012) Modeling and cyclic behavior of segmental bridge column connected with shape memory alloy bars. *Journal of Earthquake Engineering and Engineering Vibration* 11: 571–584.

Hewes JT and Priestley MJN (2002) *Seismic design and performance of precast concrete segmental bridge columns*. *Rep. No. SSRP-2001/25, Univ. of California San Diego,*. San Diego.

Kibriya LT, Málaga-Chuquitaype C, Kashani MM, et al. (2018) Nonlinear dynamics of self-centring rocking steel frames using finite element models. *Soil Dynamics and Earthquake Engineering* 115: 826–837. DOI: 10.1016/j.soildyn.2018.09.036.

Leitner EJ and Hao H (2016) Three-dimensional finite element modelling of rocking bridge piers under cyclic loading and exploration of options for increased energy dissipation. *Engineering Structures* 118: 74–88. DOI: 10.1016/j.engstruct.2016.03.042.

Li C, Hao H and Bi K (2017) Numerical study on the seismic performance of precast segmental concrete columns under cyclic loading. *Engineering Structures* 148: 373–386. DOI: 10.1016/j.engstruct.2017.06.062.

M Saiid Saiidi; Wang H (2006) Exploratory Study of Seismic Response of Concrete Columns with Shape Memory Alloys Reinforcement. *ACI Structural Journal* 103(3): 436–443.

Mander JB and Cheng CT (1997) Seismic Resistance of Bridge Piers Based on Damage Avoidance Design. *Technical Report NCEER-97-0014*: 1–148.

Marriott D, Pampanin S and Palermo A (2009) Quasi-static and pseudo-dynamic testing of unbonded post-tensioned rocking bridge piers with external replaceable dissipaters. *Earthquake Engineering and Structural Dynamics*. DOI: 10.1002/eqe.857.

McKenna F (2011) OpenSees: A Framework for Earthquake Engineering Simulation. *Computing in Science & Engineering* 13(4): 58–66. DOI: 10.1109/MCSE.2011.66.

Moon DY, Roh H and Cimellaro GP (2015) Seismic Performance of Segmental Rocking Columns Connected with NiTi Martensitic SMA Bars. *Advances in Structural Engineering* 18(4): 571–584. DOI: 10.1260/1369-4332.18.4.571.

Motaref S, Saiidi MS and Sanders DH (2010) Experimental study of precast bridge columns with built-in elastomer. *Transportation Research Record*. DOI: 10.3141/2202-14.

Motaref S, Asce AM, Saiidi MS, et al. (2014) Shake Table Studies of Energy-Dissipating Segmental Bridge Columns. *JOURNAL OF BRIDGE ENGINEERING*: 186–199. DOI: 10.1061/(ASCE)BE.1943-5592.0000518.

N. Mali AM (2017) A Review on Shape Memory Alloy and Its Application in Civil Engineering. *International Journal of Advanced Research in Science, Engineering and Technology* www.ijarset.com: 4395–4404.

Nan Gao J-SJDEH and RD (2016) An innovative seismic bracing system based on a superelastic shape memory alloy ring. *Smart Materials and Structures* 25(5).

Nikbakht E, Rashid K, Hejazi F, et al. (2015) Application of shape memory alloy bars in self-centring precast segmental columns as seismic resistance. *Structure and Infrastructure Engineering* 11(3): 297–309. DOI: 10.1080/15732479.2013.876056.

Ou YC, Chiewanichakorn M, Aref AJ, et al. (2007) Seismic performance of segmental precast unbonded posttensioned concrete bridge columns. *Journal of Structural Engineering*. DOI: 10.1061/(ASCE)0733-9445(2007)133:11(1636).

Ou Y-C, Tsai M-S, Chang K-C, et al. (2010) Cyclic behavior of precast segmental concrete bridge columns with high performance or conventional steel reinforcing bars as energy dissipation bars. *Earthquake Engineering & Structural Dynamics* 39(11). DOI: 10.1002/eqe.986.

Pereiro-Barceló J, L.Bonet J, Cabañero-Escudero B, et al. (2019) Cyclic behavior of hybrid RC columns using High-Performance Fiber-Reinforced Concrete and Ni-Ti SMA bars in critical regions. *Composite Structures* 212: 207–219.

Roh H and Reinhorn AM (2010) Hysteretic behavior of precast segmental bridge piers with superelastic shape memory alloy bars. *Engineering Structures* 32(10). Elsevier Ltd: 3394–3403. DOI: 10.1016/j.engstruct.2010.07.013.

S. Saiidi MO and MS-Z (2009) Cyclic Response of Concrete Bridge Columns Using Superelastic Nitinol and Bendable Concrete. *ACI Structural Journal* 106(1): 69–77.

S. Varela MSS (2014) Dynamic Performance of Novel Bridge columns with superelastic CuAlMn shape memory alloy and ECC. *International Journal of Bridge Engineering* 2: 29–58.

Sherif MM, Khakimova EM, Tanks J, et al. (2018) Cyclic flexural behavior of hybrid SMA/steel fiber reinforced concrete analyzed by optical and acoustic techniques. *Composite Structures* 201: 248–260. DOI: 10.1016/j.compstruct.2018.06.039.

Shim CS, Chung C-H and Kim HH (2008) Experimental evaluation of seismic performance of precast segmental bridge piers with a circular solid section. *Engineering Structures* 30(12). DOI: 10.1016/j.engstruct.2008.07.005.

Shrestha B and Hao H (2016) Parametric study of seismic performance of super-elastic shape memory alloy-reinforced bridge piers. *Structure and Infrastructure Engineering* 12(9): 1076–1089. DOI: 10.1080/15732479.2015.1076856.

Song G, Ma N and Li H-N (2006) Applications of shape memory alloys in civil structures. *Engineering Structures* 28(9): 1266–1274. DOI: 10.1016/j.engstruct.2005.12.010.

Speicher MS, DesRoches R and Leon RT (2011) Experimental results of a NiTi shape memory alloy (SMA)-based recentering beam-column connection. *Engineering Structures* 33(9): 2448–2457. DOI: 10.1016/j.engstruct.2011.04.018.

Spieth HA, Carr AJ, Murahidy AG, et al. (2004) Modelling of post-tensioned precast reinforced concrete frame structures with rocking beam-column connections. In: *New Zealand society of earthquake engineering Conference 2004*, 2004.

Suhail R, Amato G and McCrum DP (2020) Active and passive confinement of shape modified low strength concrete columns using SMA and FRP systems. *Composite Structures* 251: 112649. DOI: 10.1016/j.compstruct.2020.112649.

Tazarv M and Saiid Saiidi M (2015) Reinforcing NiTi Superelastic SMA for Concrete Structures. *Journal of Structural Engineering* 141(8): 04014197. DOI: 10.1061/(ASCE)ST.1943-541X.0001176.

Tazarv M and Saiid Saiidi M (2016) Low-Damage Precast Columns for Accelerated Bridge Construction in High Seismic Zones. *Journal of Bridge Engineering* 21(3). DOI: 10.1061/(ASCE)BE.1943-5592.0000806.

Varela S and 'Saiid' Saiidi M (2016) A bridge column with superelastic NiTi SMA and replaceable rubber hinge for earthquake damage mitigation. *Smart Materials and Structures* 25(7): 075012. DOI: 10.1088/0964-1726/25/7/075012.

Varela S and Saiidi M (2017) Resilient deconstructible columns for accelerated bridge construction in seismically active areas. *Journal of Intelligent Material Systems and Structures* 28(13): 1751–1774. DOI: 10.1177/1045389X16679285.

Wilson JC and Wesolowsky MJ (2005) Shape Memory Alloys for Seismic Response Modification: A State-of-the-Art Review. *Earthquake Spectra* 21(2): 569–601. DOI: 10.1193/1.1897384.

Z.B. Haber (2013) *Precast Column-Footing Connections for Accelerated Bridge Construction in Seismic Zones, ProQuest Dissertations and Theses.*

Accepted manuscript doi:
10.1680/jstbu.22.00219

Table 1. SMA parameters used in this study [21].

| Parameters | Description | Value |
|---|---|---|
| $E$ | Initial modulus of elasticity | 68.2 GPa |
| $\varepsilon_L$ | Volumetric transformation strain | 0.06 |
| $\sigma_{sAM}$ | Start stress at austenite-to-martensite transformation phase | 480 MPa |
| $\sigma_{fAM}$ | Finish stress at austenite-to-martensite transformation phase | 540 MPa |
| $\sigma_{sMA}$ | Start stress at martensite-to-austenite transformation phase | 260 MPa |
| $\sigma_{fMA}$ | Finish stress at martensite-to-austenite transformation phase | 120 MPa |

Table 2. Values of design parameters

| Design Parameters | $n$ | $N/(f_cA_c)$ | $\alpha_t$ | $\rho_t$ | $J_{sma}$ | $\alpha_{sma}$ | $\rho_{sma}$ |
|---|---|---|---|---|---|---|---|
| Values | 2 | 0.2 | 0.0 | 0.010 | 2 | 0.0 | 0.005 |
| | 4 | 0.2 | 0.2 | 0.015 | 3 | 0.3 | 0.01 |
| | 6 | 0.2 | 0.4 | 0.020 | 4 | 0.6 | 0.015 |
| | 10 | 0.2 | 0.6 | - | 5 | - | 0.025 |

Table 3. Representative piers for dynamic analyses

| Piers | $\alpha_t$ | $\rho_t$ | $\alpha_{sma}$ | $\rho_{sma}$ | $f_n$ (Hz) |
|---|---|---|---|---|---|
| A0 | 0.6 | 0.020 | 0.0 | 0.0 | 3.80 |
| A1 | 0.6 | 0.020 | 0.6 | 0.025 | 3.96 |
| A2 | 0.6 | 0.020 | 0.3 | 0.025 | 3.96 |
| B0 | 0.4 | 0.020 | 0.0 | 0.00 | 3.80 |
| B1 | 0.4 | 0.020 | 0.3 | 0.025 | 3.95 |
| B2 | 0.4 | 0.020 | 0.6 | 0.025 | 3.95 |
| C0 | 0.2 | 0.020 | 0.0 | 0.00 | 3.80 |
| C1 | 0.2 | 0.020 | 0.6 | 0.025 | 3.96 |
| C2 | 0.2 | 0.020 | 0.3 | 0.025 | 3.96 |

Accepted manuscript doi:
10.1680/jstbu.22.00219

**Figure captions**

Fig. 1. The exemplary bridge pier: (a) geometry of the pier, (b) arrangement of the SMA bars, (c) tendon's location only, and (d) FE model in OpenSees.

Fig. 2. Modelling details of the joints: (a) base joint (see J1 in Fig. 1), (b) intermediate joint (see J2 in Fig. 1), and (c) positioning of the vertical elements/springs for an intermediate joint.

Fig. 3. Idealized constitutive model of SMA material implemented by the authors in OpenSees.

Fig. 4. Effects of SMA bars' length ($\alpha_t$ = 0.4, $\rho_t$ = 0.01, $\alpha_{sma}$ = 0.3, $\rho_{sma}$ = 0.01) for the piers with: (a) $n$ = 2, (b) $n$ = 4, (c) $n$ = 6, and (d) $n$ = 8.

Fig. 5. Effects of SMA bars' area for the pier with $n$ = 4, $\alpha_t$ = 0.4, $\rho_t$ = 0.01, $\alpha_{sma}$ = 0.3: (a) $J_{sma}$ = 2, (b) $J_{sma}$ = 3, and (c) $J_{sma}$ = 4

Fig. 6. (a) Post-tensioning effect of the SMA bars on the energy dissipation capacity of the exemplary pier ($n$ = 4, $\alpha_t$ = 0.4, $\rho_t$ = 0.015, $J_{sma}$ = 3); the corresponding stress-strain behaviour of the SMA bars for: (b) $\alpha_{sma}$ = 0, (c) $\alpha_{sma}$ = 0.3, and (d) $\alpha_{sma}$ = 0.6.

Fig. 7. Effects of (a) post-tensioning ($n$ = 4, $\alpha_{sma}$ = 0.3, $\rho_t$ = 0.01, $\rho_{sma}$ = 0.01, $J_{sma}$ = 3), and (b) area of the tendon ($n$ = 4, $\alpha_{sma}$ = 0.3, $\alpha_t$ = 0.4, $\rho_{sma}$ = 0.01, $J_{sma}$ = 3) on the energy dissipation capacity of the exemplary pier.

Fig. 8. Dissipated Energy of the exemplary pier ($n$ = 4, $\alpha_{sma}$ = 0.3, $J_{sma}$ = 3) for: (a) $\rho_t$ = 0.010, (b) $\rho_t$ = 0.015, and (c) $\rho_t$ = 0.020.

Fig. 9. Hysteresis curves for the pier B0 (no SMA bars) and pier B1 (SMA-equipped) subject to sinusoidal loading frequency of 2.1 Hz and amplitude: (a) 0.1g, (b) 0.2g, (c) 0.3g. (g is gravitational acceleration)

Fig. 10. An example of FRF extraction steps for loading amplitude of 0.005g for Pier B2 (a) full acceleration response time- history, (b) isolated steady-state acceleration response, and (c) conversion of time domain to frequency domain.

Fig. 11. Frequency response functions (FRFs) for the acceleration response (a) Pier A0, (b) Pier A1, (c) Pier A2, (d) Pier B0, (e) Pier B1, (f) Pier B2, (g) Pier C0, (h) Pier C1, and (i) Pier C2.

Fig. 12. Frequency response functions (FRFs) for the drift response (a) Pier A0, (b) Pier A1, (c) Pier A2, (d) Pier B0, (e) Pier B1, (f) Pier B2, (g) Pier C0, (h) Pier C1, and (i) Pier C2.

Fig. 13. Comparison of the backbone curves for piers given in Table 3.

Accepted manuscript doi:
10.1680/jstbu.22.00219

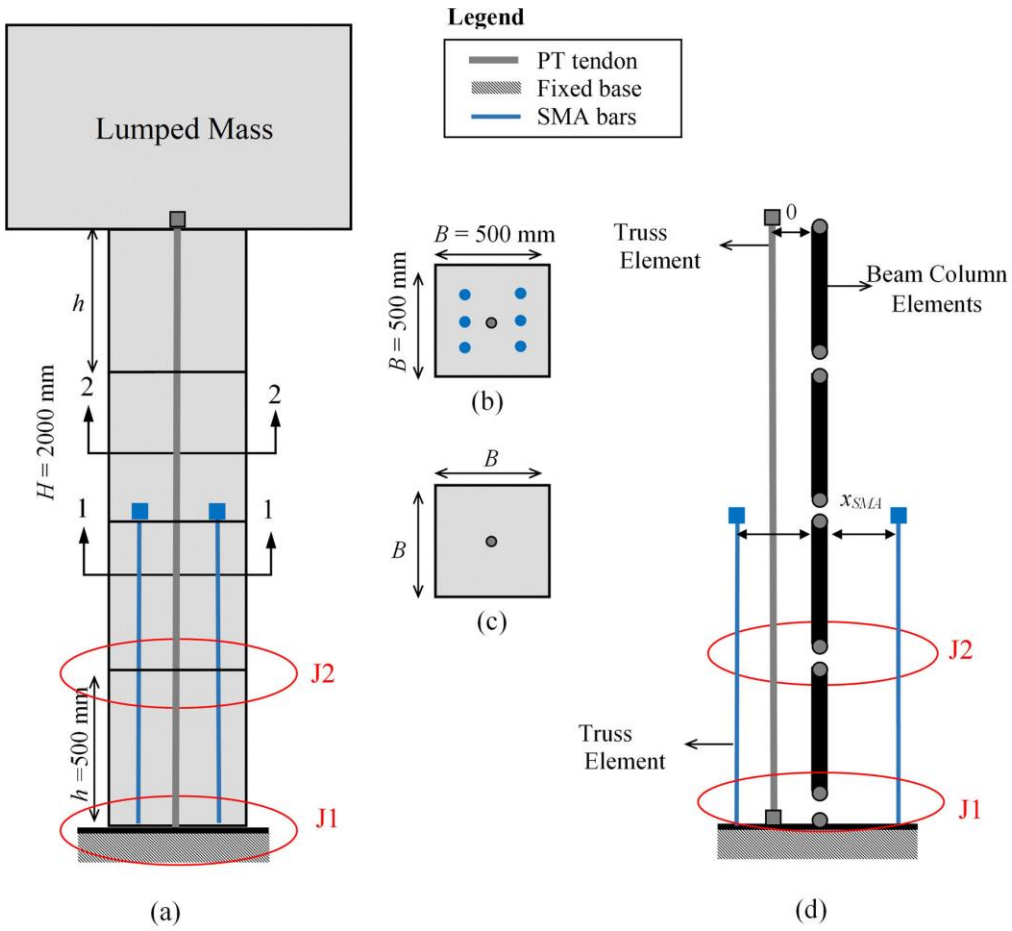


Figure1

Accepted manuscript doi:
10.1680/jstbu.22.00219

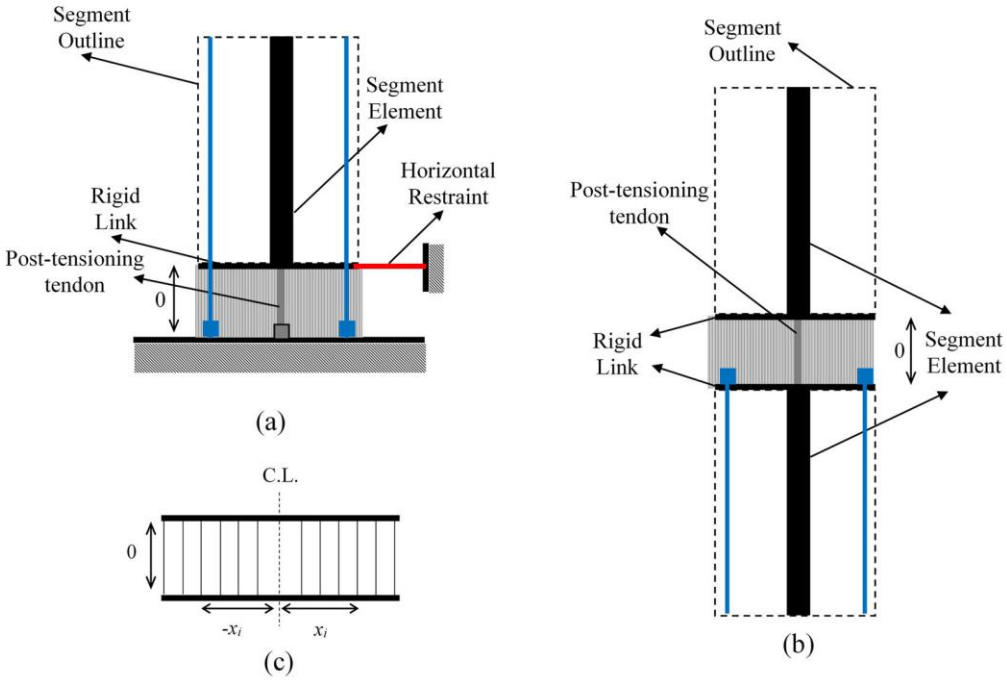


Figure2

Accepted manuscript doi:
10.1680/jstbu.22.00219

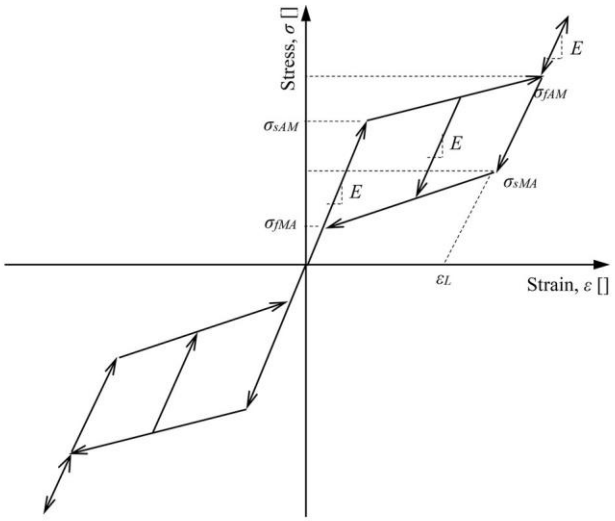


Figure3

Accepted manuscript doi:
10.1680/jstbu.22.00219

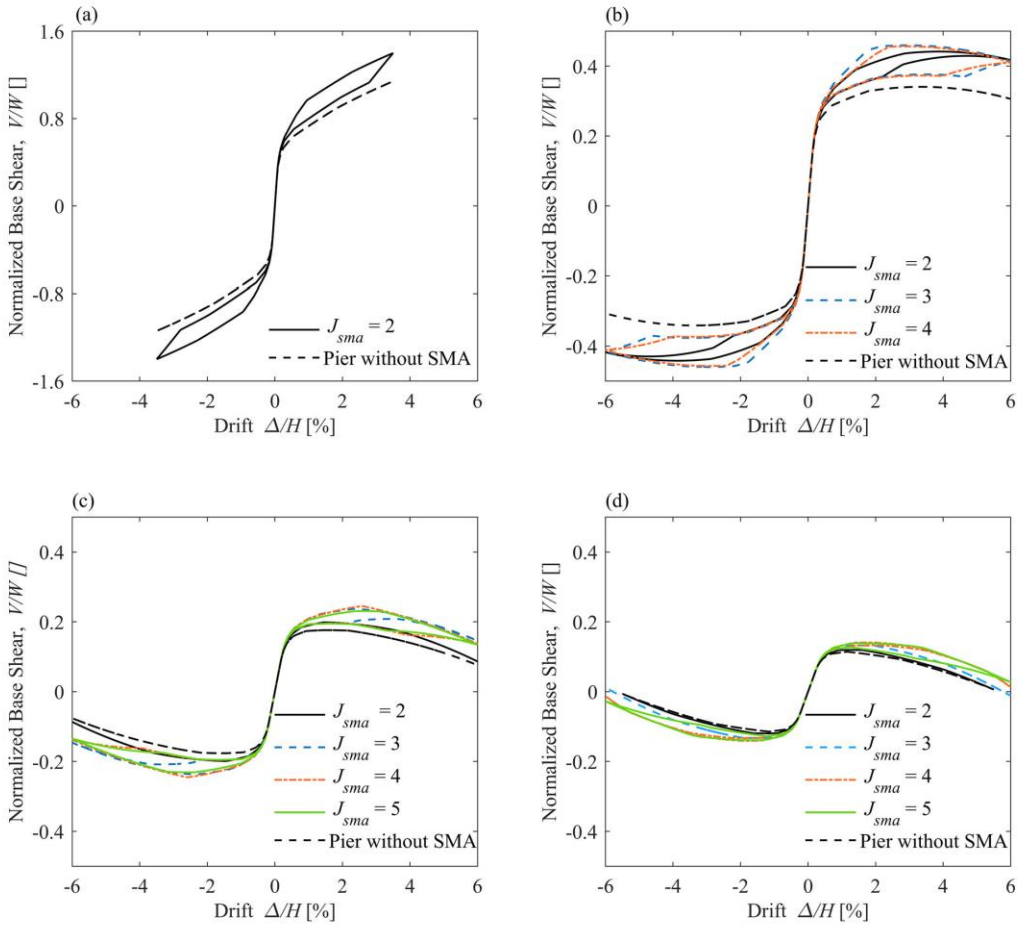


Figure4

Accepted manuscript doi:
10.1680/jstbu.22.00219

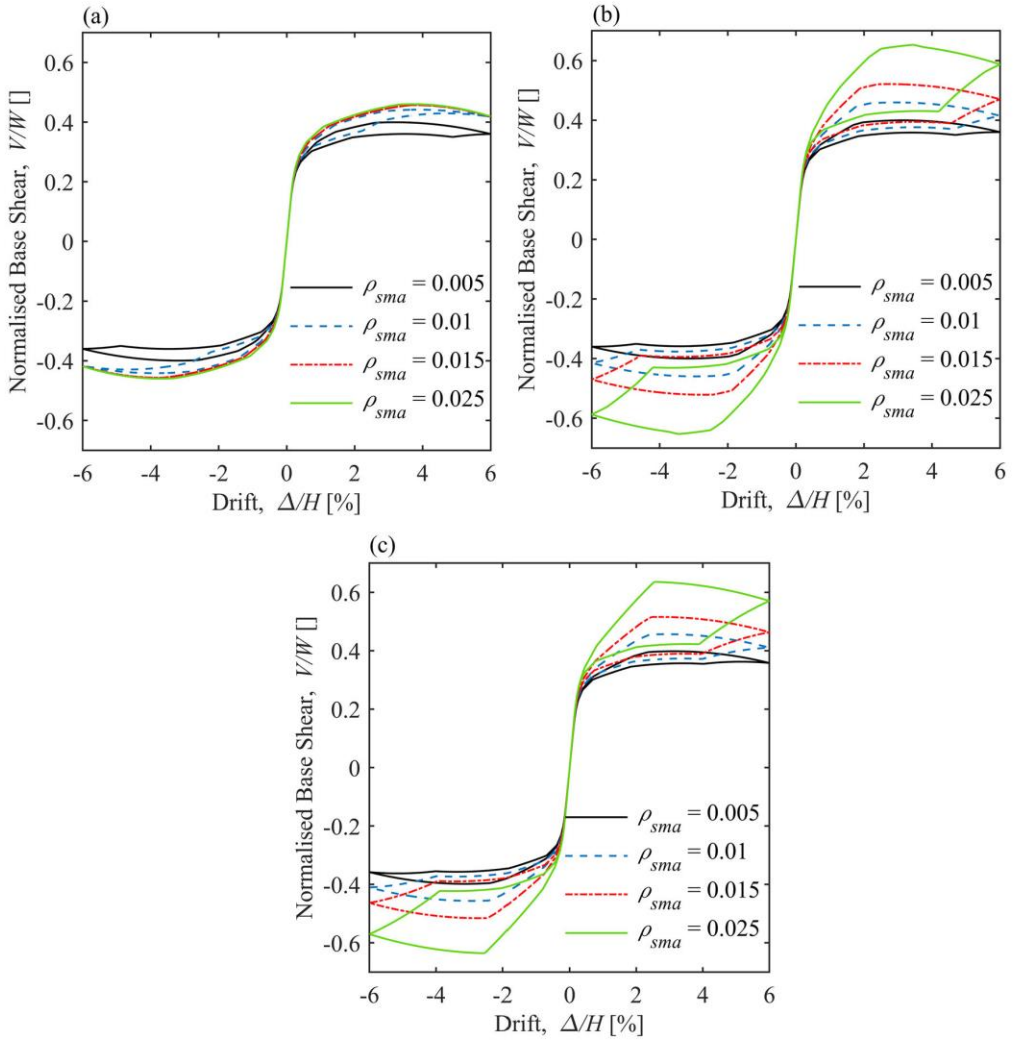


Figure5

Accepted manuscript doi:
10.1680/jstbu.22.00219

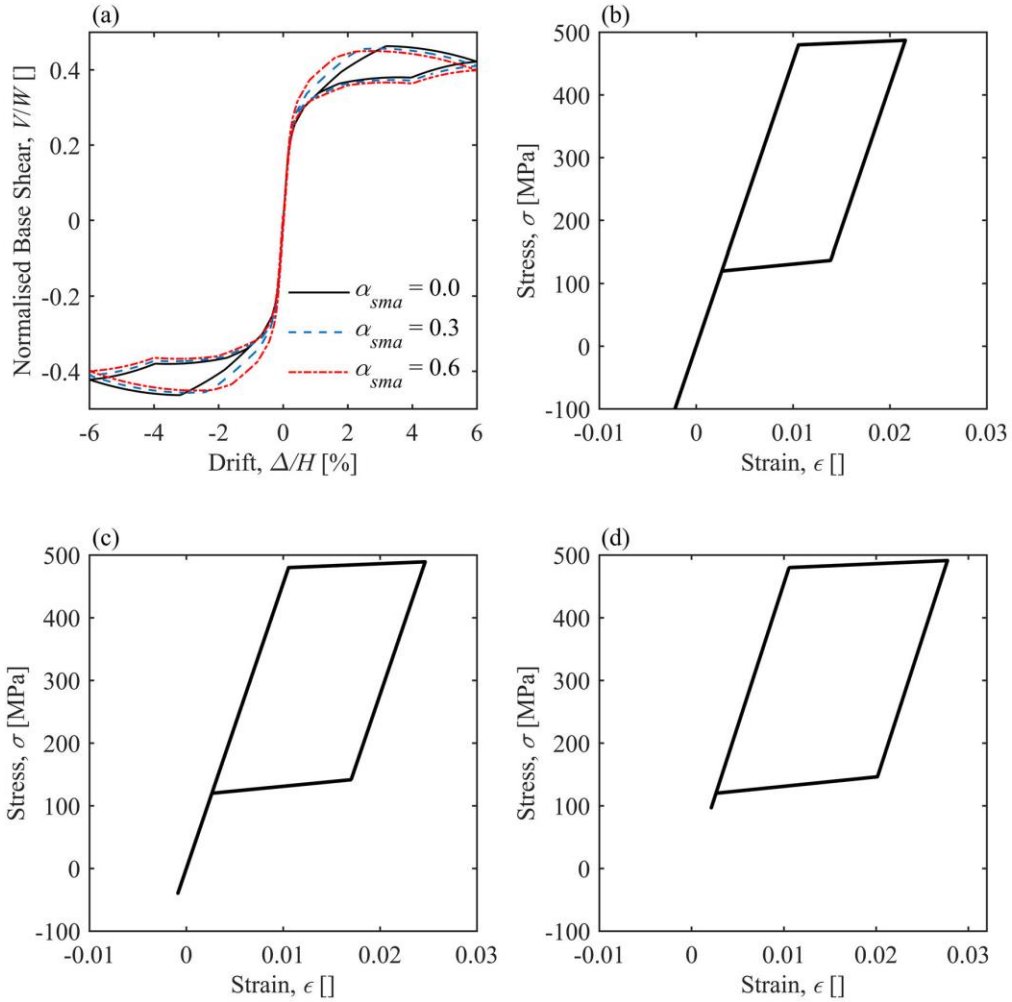


Figure6

Accepted manuscript doi:
10.1680/jstbu.22.00219

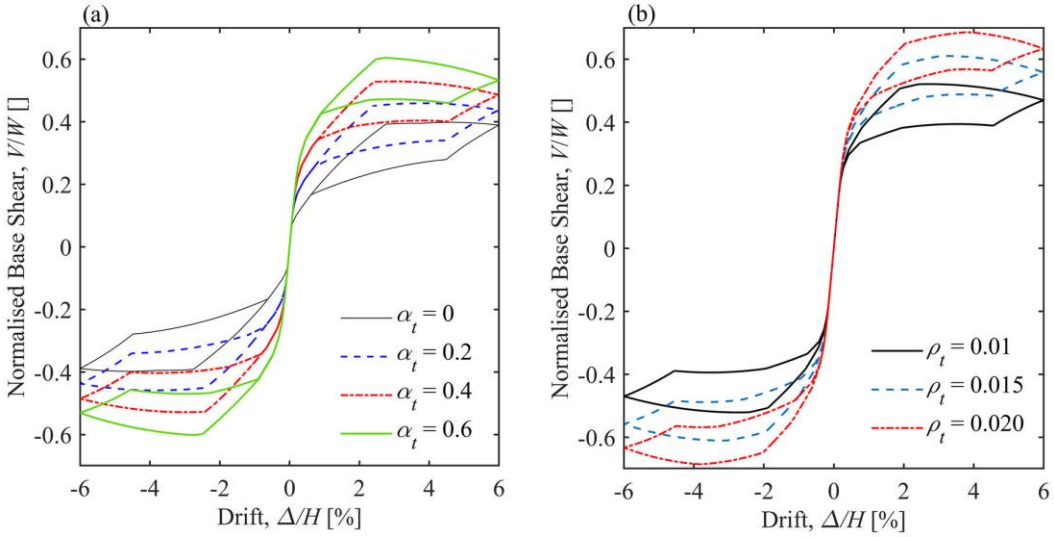


Figure7

Accepted manuscript doi:
10.1680/jstbu.22.00219

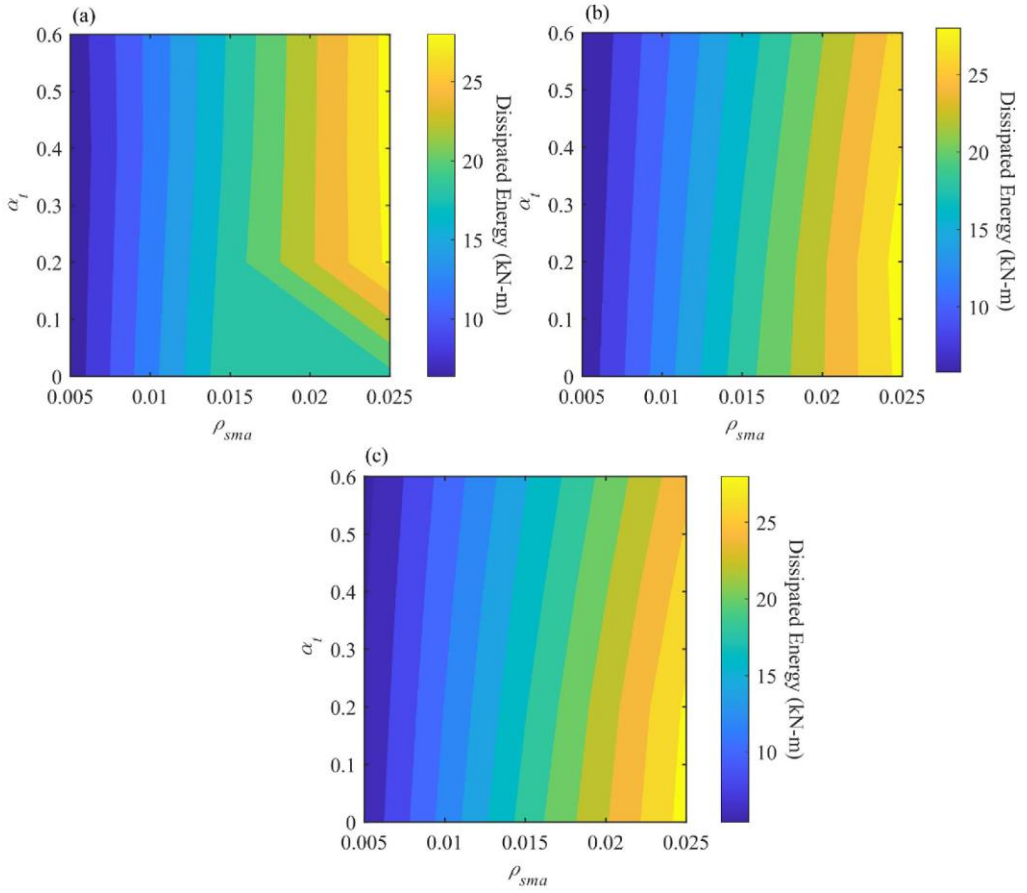


Figure8

Accepted manuscript doi:
10.1680/jstbu.22.00219

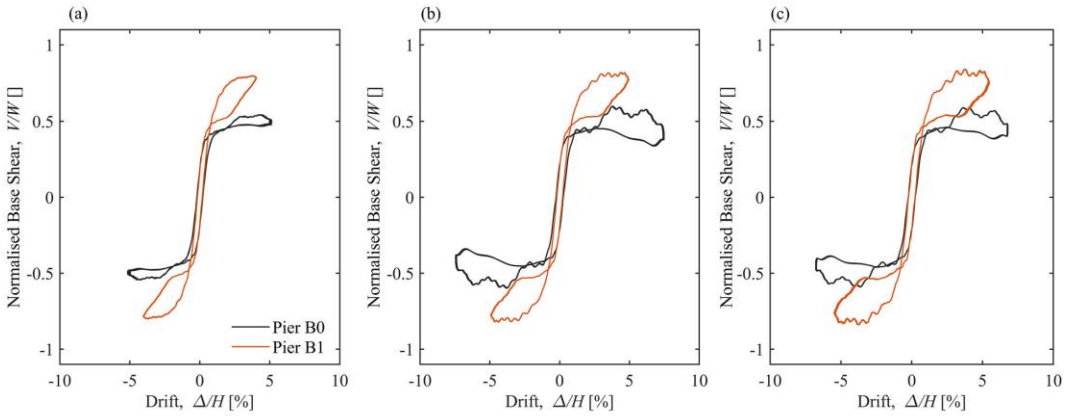


Figure9

Accepted manuscript doi:
10.1680/jstbu.22.00219

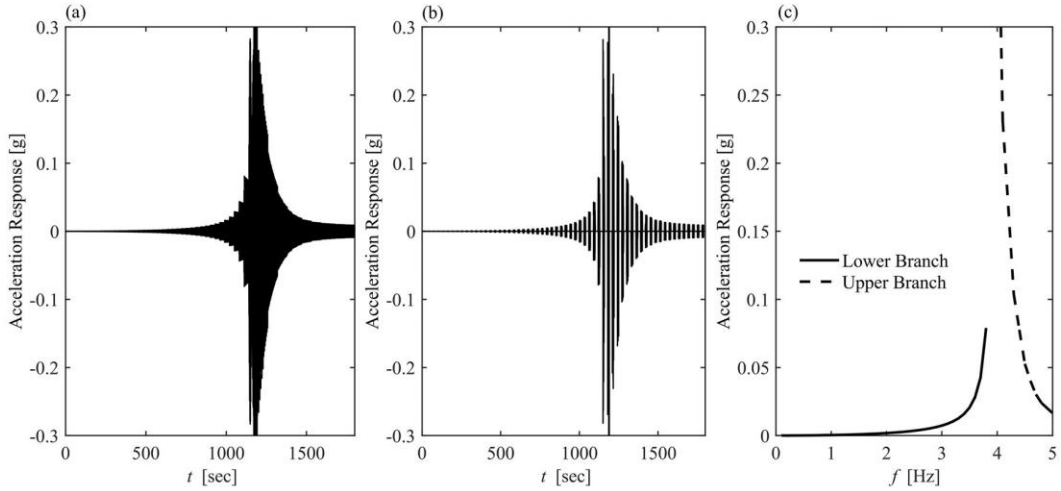


Figure10

Accepted manuscript doi:
10.1680/jstbu.22.00219

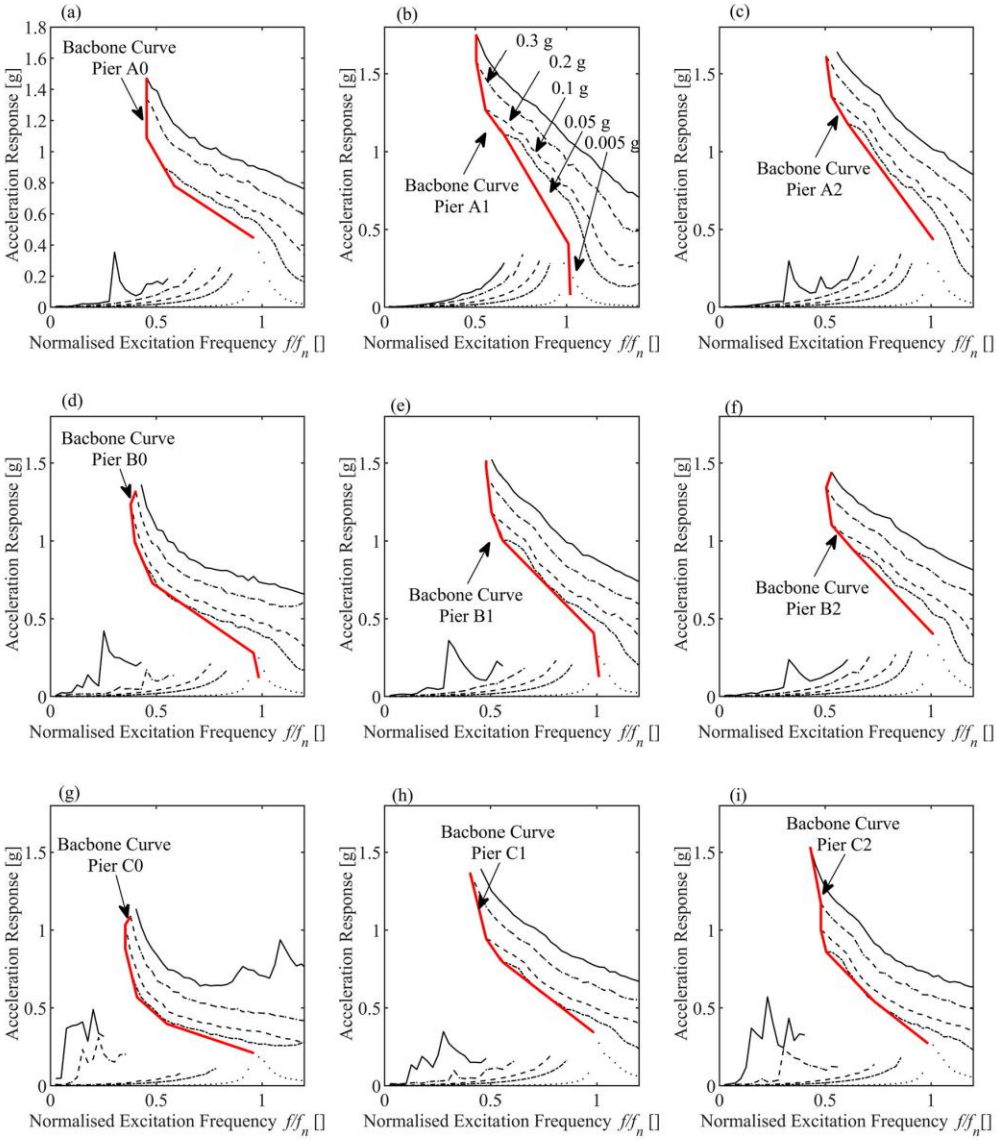


Figure11

Accepted manuscript doi:
10.1680/jstbu.22.00219

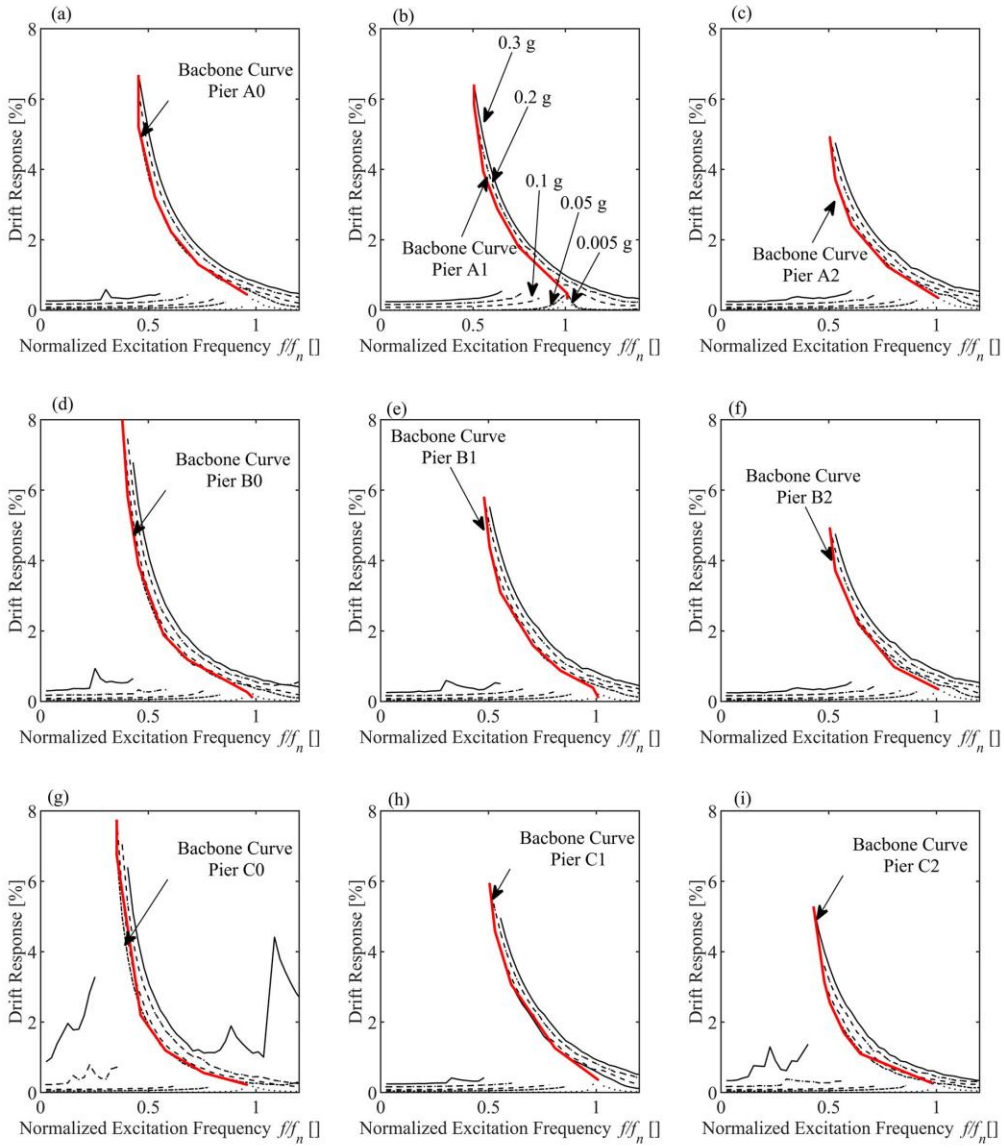


Figure12

Accepted manuscript doi:
10.1680/jstbu.22.00219

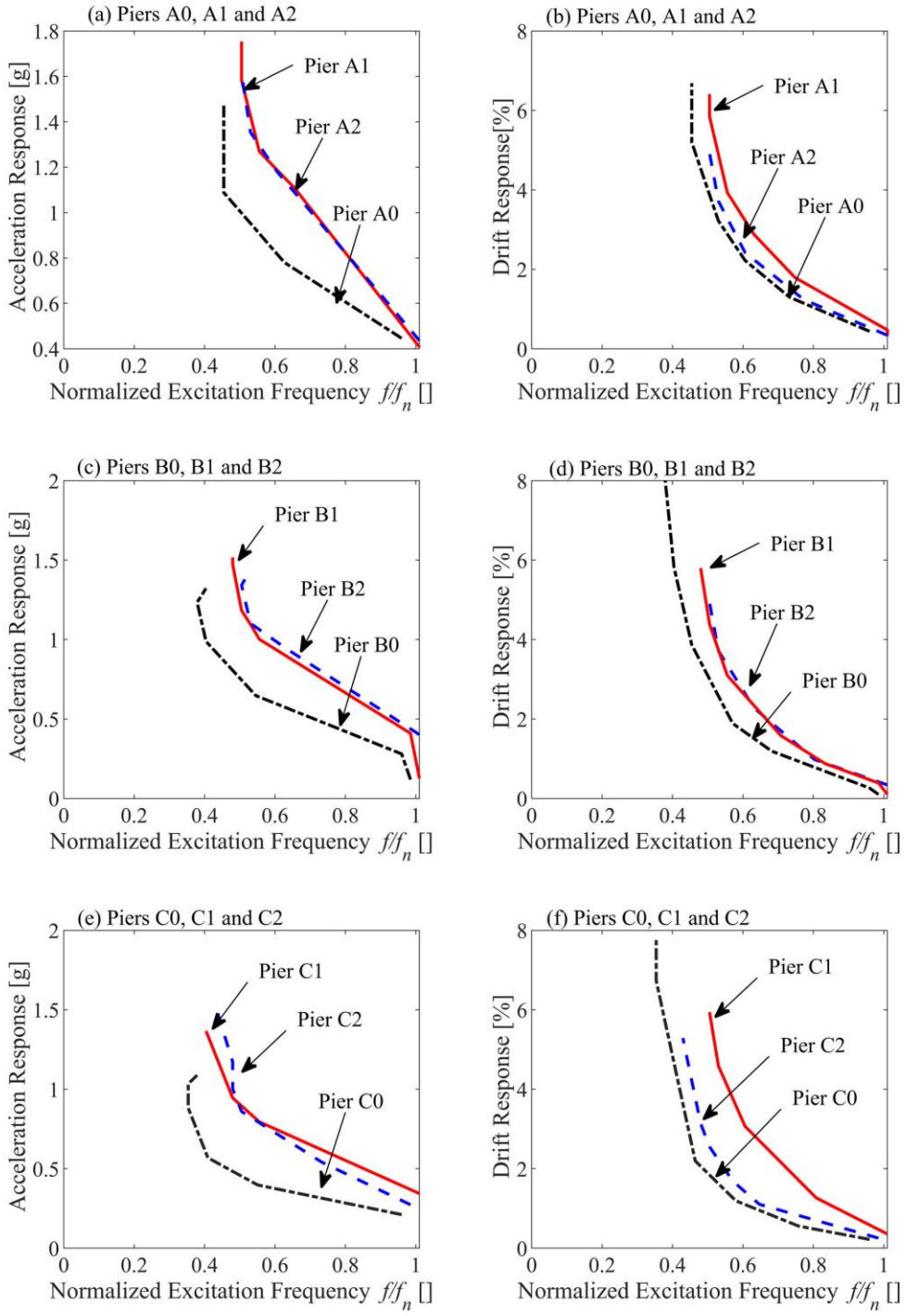


Figure13